

Supplementary Materials for

Soft-bodied adaptive multimodal locomotion strategies in fluid-filled confined spaces

Ziyu Ren, Rongjing Zhang, Ren Hao Soon, Zemin Liu, Wenqi Hu*, Patrick R. Onck*, Metin Sitti*

*Corresponding author. Email: wenqi@is.mpg.de (W.H.); P.R.Onck@rug.nl (P.R.O.); sitti@is.mpg.de (M.S.)

Published 30 June 2021, *Sci. Adv.* **7**, eabh2022 (2021)
DOI: 10.1126/sciadv.abh2022

The PDF file includes:

Tables S1 and S2
Figs. S1 to S15
Legends for movies S1 to S8

Other Supplementary Material for this manuscript includes the following:

(available at advances.sciencemag.org/cgi/content/full/7/27/eabh2022/DC1)

Movies S1 to S8

Figure	Material for test environment	Fluid	δ or γ	Robot length	$ \vec{B} $ and f
Fig. 1B i	UV curable resin BV-007A	720 cSt (Glycerol solution)	$\delta=1.1$	5.5 mm	10 mT, 1 Hz
Fig. 1B ii	UV curable resin BV-007A	720 cSt (Glycerol solution)	$\delta=7.33$	5.5 mm	40 mT, 1 Hz
Fig. 1B iii	UV curable resin BV-007A	720 cSt (Glycerol solution)	$\gamma=3.43$	5.5 mm	40 mT, 3 Hz
Fig. 2A	UV curable resin BV-007A	343 cSt (Glycerol solution)	$\delta=4.67$	3.5 mm	40 mT, 1 Hz and 10 Hz
Fig. 2C	UV curable resin BV-007A	6cSt, 343 cSt, and 720 cSt (Glycerol solution)	$\delta=4.67$	3.5 mm	40 mT, 1 – 10 Hz
Fig. 3A	UV curable resin BV-007A	343 cSt (Glycerol solution)	$\delta=7, 4.67,$ and 3.5	3.5 mm	40 mT, 1 Hz and 10 Hz
Fig. 3B	UV curable resin BV-007A	343 cSt (Glycerol solution)	$\delta=4.67, 9.33,$ and 14	3.5, 7, and 10.5 mm	40 mT, 1 – 10 Hz
Fig. 3C	Mold max 20	720 cSt (Glycerol solution)	$\delta=4.67$	3.5 mm	40 mT, 1 Hz
Fig. 4A	UV curable resin BV-007A	6cSt (Glycerol solution)	$\delta=7.33$	5.5 mm	40 mT, 1 Hz
Fig. 4B	UV curable resin BV-007A	6cSt (Glycerol solution)	$\delta=7.33$	5.5 mm	40 mT, 1 Hz

Fig. 4C	Mold max 20	343 cSt (Glycerol solution)	$4.12 \leq \delta \leq 7$	5.5 mm	40 mT, 1 Hz and 8 Hz
Fig. 5A	PDMS	water	$\gamma = 2.5$	4 mm	40 mT, 10 Hz
Fig. 5B	Tygon® formula 2375 laboratory tubing	720 cSt (Glycerol solution)	$\gamma = 2.81$	4.5 mm	40 mT, 1 Hz
Fig. 6A	PDMS	720 cSt (Glycerol solution)	$2.2 \leq \gamma \leq 5.3$	3.5 – 8.5 mm	40 mT, 3 Hz
Fig. 6B	PDMS	720 cSt (Glycerol solution)	$\gamma = 2.81$	4.5 mm	45 mT, 3Hz
Fig. 6C	PDMS	720 cSt (Glycerol solution)	$\gamma = 2.5, 5,$ and 7.5	4, 8, and 12 mm	40 mT, 3Hz
Fig. 7	UV curable resin BV-007A and Tygon® formula 2375 laboratory tubing	Shear-thinning fluid (hyaluronic acid sodium solution)	$\delta \leq 7,$ $\gamma \geq 2.81$	4.5 mm	Indicated in Fig. 7
Fig. S5	UV curable resin BV- 007A	Indicated in Fig. S5	Indicated in Fig. S5	3.5 mm	40 mT, 1-10 Hz
Fig. S8	PDMS	343 cSt (Glycerol solution)	-	3.5 mm	40 mT, 1 Hz
Fig. S9	UV curable resin BV-007A	343 cSt (Glycerol solution), flow speed 1 mm/s	$\delta = 4.67$	3.5 mm	40 mT, 1 Hz and 3 Hz
Fig. S11	UV curable resin BV-007A	Indicated in Fig. S11	Indicated in Fig. S11	3.5 mm – 8.5 mm	40 mT, 3 Hz

Fig. S14	UV curable resin BV-007A	343 cSt (Glycerol solution) and Shear-thinning fluid	$\delta=4.67$	3.5 mm	40 mT, 10 Hz
----------	-----------------------------	--	---------------	--------	--------------

Table S1. Experimental conditions at which the experimental data are obtained in each figure of this study.

Polymer matrix	25% strain modulus (kPa)
Ecoflex 0010	19 ± 1
Dragon skin 30	710 ± 7
PDMS	2065 ± 25

Table S2. The modulus of the magnetic composite material with different polymer matrixes. The magnetic composite materials were fabricated by mixing the NdFeB powder and the corresponding polymer with a mass ratio of 1:1. The modulus was measured by tensile testing.

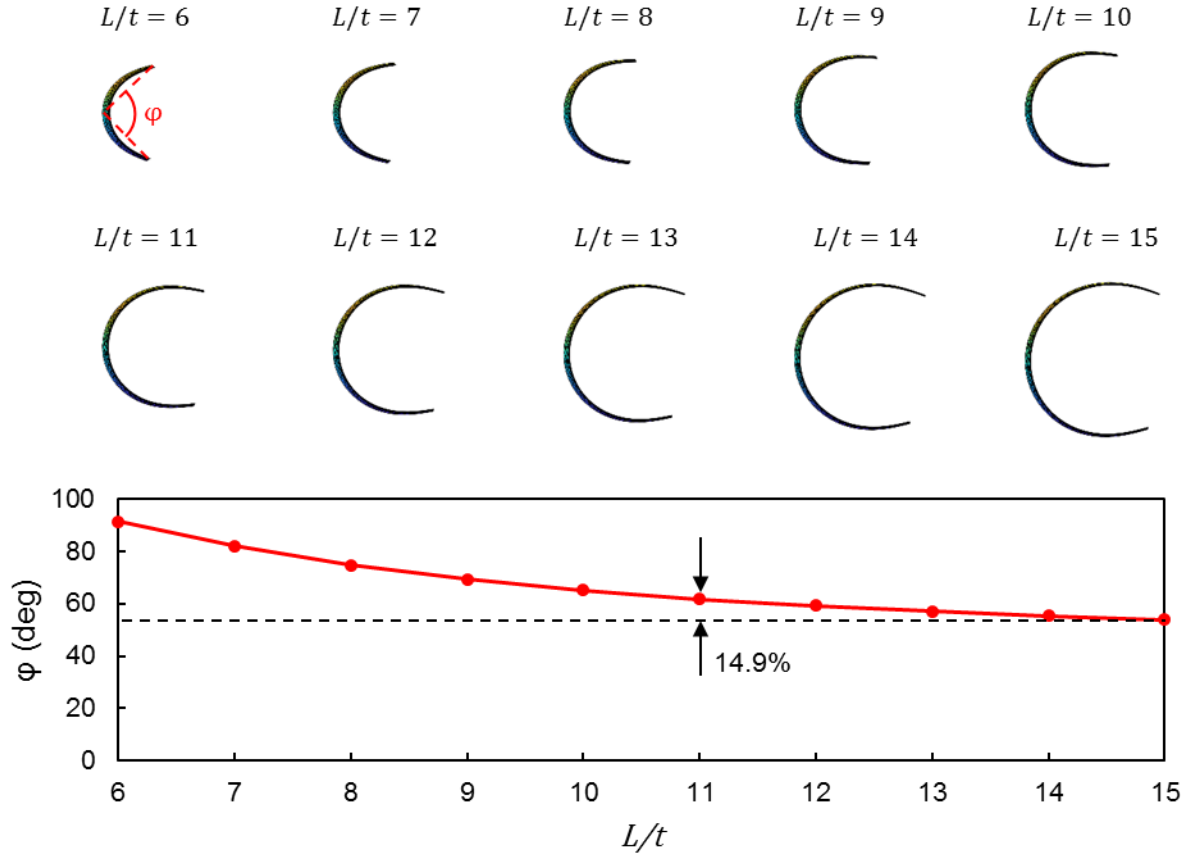


Fig. S1. The influence of the length-to-thickness ratio on the simulated robot deformation. In the simulations, a constant \vec{B} ($|\vec{B}|=40$ mT) is provided to let the virtual robot curl into a C shape. L is the robot length, and $t=240$ μm is the robot thickness. The deformation of the robot can be characterized by the angle ϕ . A larger ϕ indicates a smaller deformation. The black dashed line in the bottom figure indicates the value of ϕ achieved for $L/t=15$. The value of ϕ asymptotically decreases to this value with increasing L/t . The ϕ achieved at $L/t=11$ is 14.9% larger than this asymptotical value. When L/t becomes smaller than 11, the deformation progressively decreases.

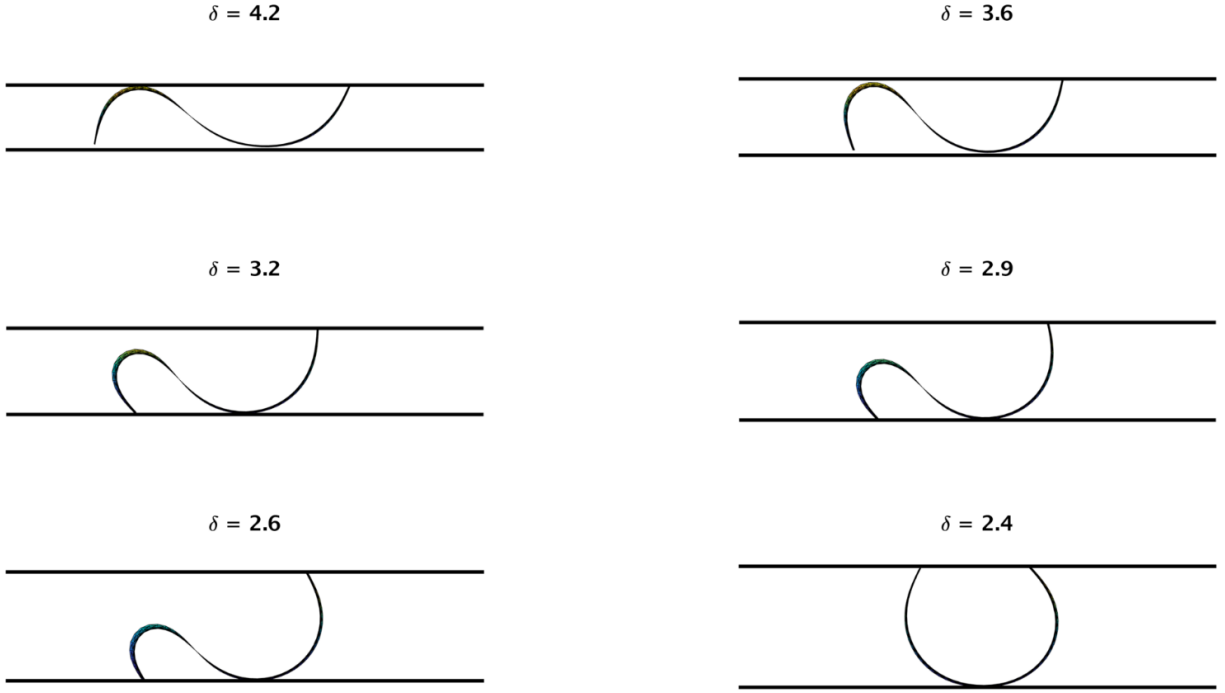


Fig. S2. Determining small and big gaps using δ . In the simulations, a constant $\bar{\mathbf{B}}$ ($|\mathbf{B}|=40$ mT) is applied to let the robot deform into a sinusoidal shape in the gap. δ is varied by changing the gap width. When δ is smaller than 2.6, the robot will not be able to deform into the sinusoidal shape due to the lack of boundary restriction, and the undulatory travelling wave cannot be produced. Therefore, we use the term ‘small gap’ for δ values larger than 2.6, and ‘big gap’ for δ values smaller than 2.6.

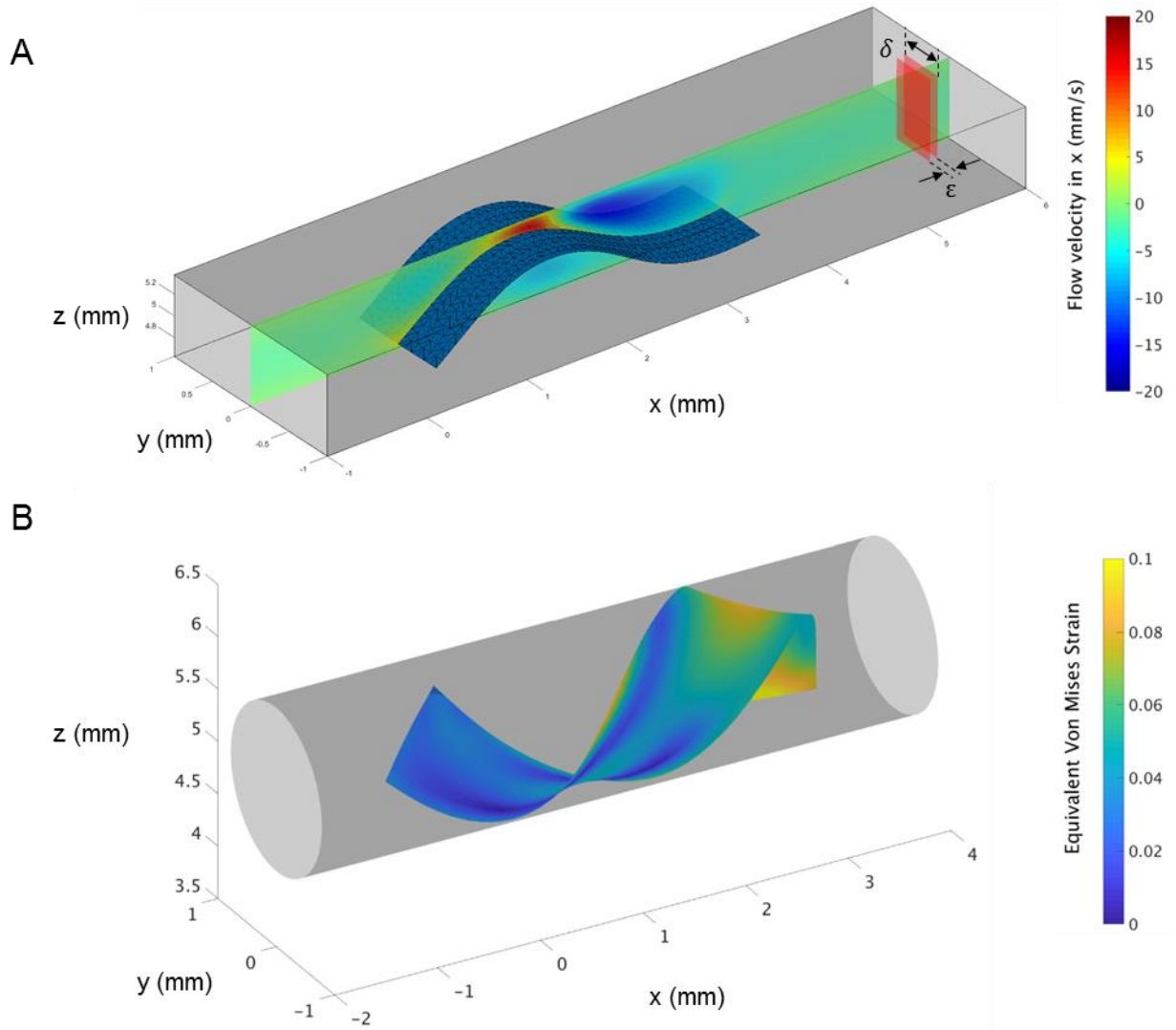


Fig. S3. The simulated sheet-shaped soft robot in different geometrical environments. The boundaries, robots, and the fluid domain are meshed by triangular elements. (A) The virtual robot is performing undulatory locomotion. The flow field is analyzed in the mid-sagittal plane of the robot as shown in the figure. In the simulation shown here, the robot has a length of 3.5 mm, and the channel has dimensions of $10 \times 0.75 \times 2$ mm. The volume marked with the red shade is the region used to calculate the normalized net flow. We select $\delta = 0.05$ mm and $\epsilon = 0.5$ mm. (B) The virtual robot is performing helical surface crawling. In the simulation shown here, the robot has a length of 5.5 mm, and the tube has a diameter of 1.6 mm.

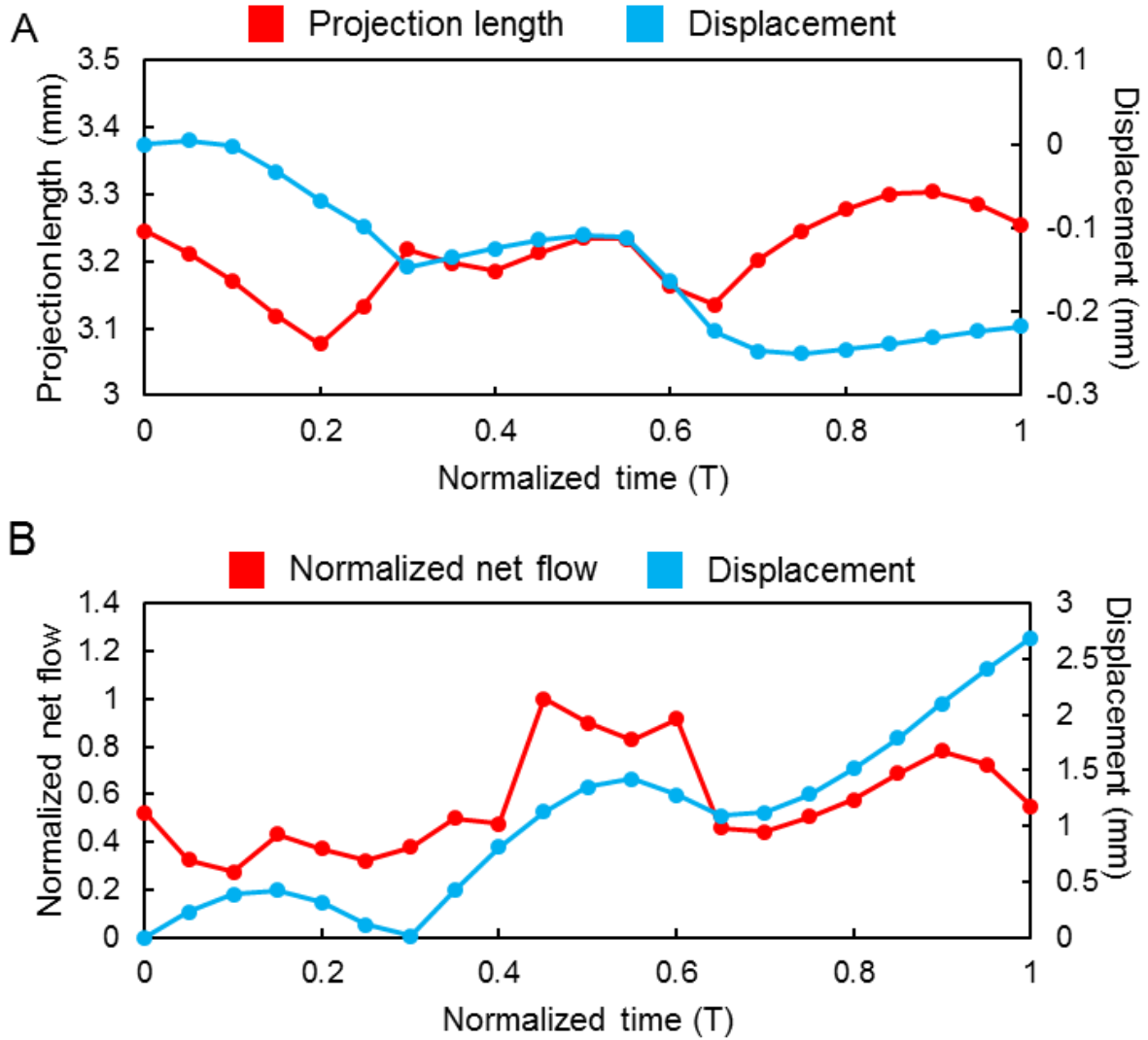


Fig. S4. The physical mechanism of the undulatory crawling and swimming modes. (A) The variation of the projection length correlates to the variation of the robot displacement, indicating that the robot net displacement is the result of the cyclic changing of the robot projection length. Note that an increase and decrease of the projection length can both increase the displacement. (B) The variation of the normalized net flow roughly matches the variation of the robot displacement, indicating that the thrust is produced by transporting the fluid. In (A) and (B), the displacement of the middle point of the projection length is measured. All data are obtained from the CFD simulations.

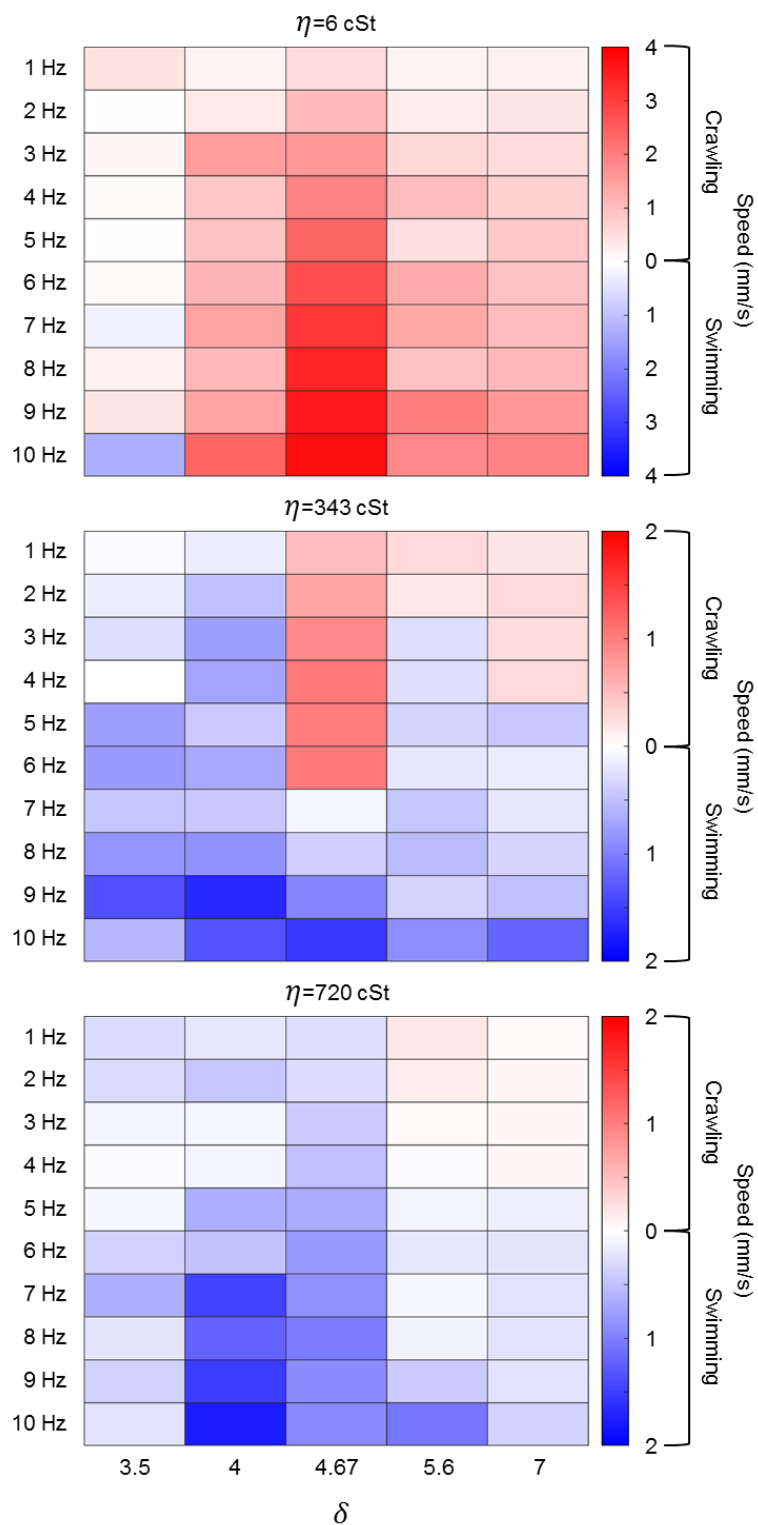


Fig. S5. Parameter sweeping experiments on the undulatory locomotion. The strength of the magnetic field is 40 mT in all cases.

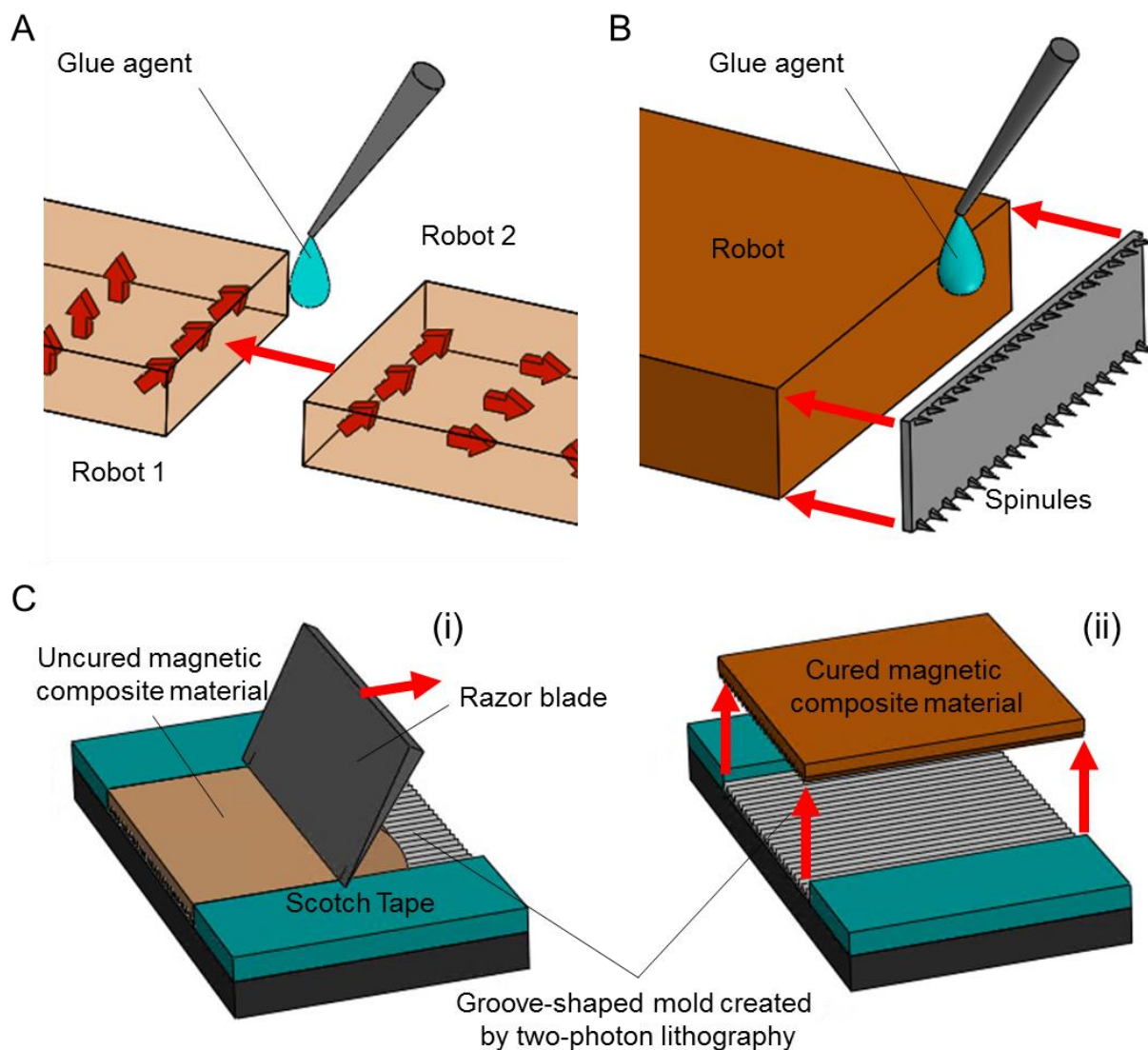


Fig. S6. Fabricating the sheet-shaped soft millirobots with grooves, spinules, and multi-wavelength sinusoidal magnetization profiles. (A) Two robots are connected in series by applying glue agents (uncured Ecoflex 00-10) to create multi-period sinusoidal magnetization profiles. (B) The spinules are integrated to the leading and the trailing edges of the sheet-shaped robot by applying glue agents (uncured Ecoflex 00-10). (C) The fabrication of the grooved film made of magnetic composite material. (i) Uncured magnetic composite material is daubed on a grooved mold and flattened using a razor blade. (ii) The sheet of the cured magnetic composite material is picked up from the grooved mold for the following fabrication steps.

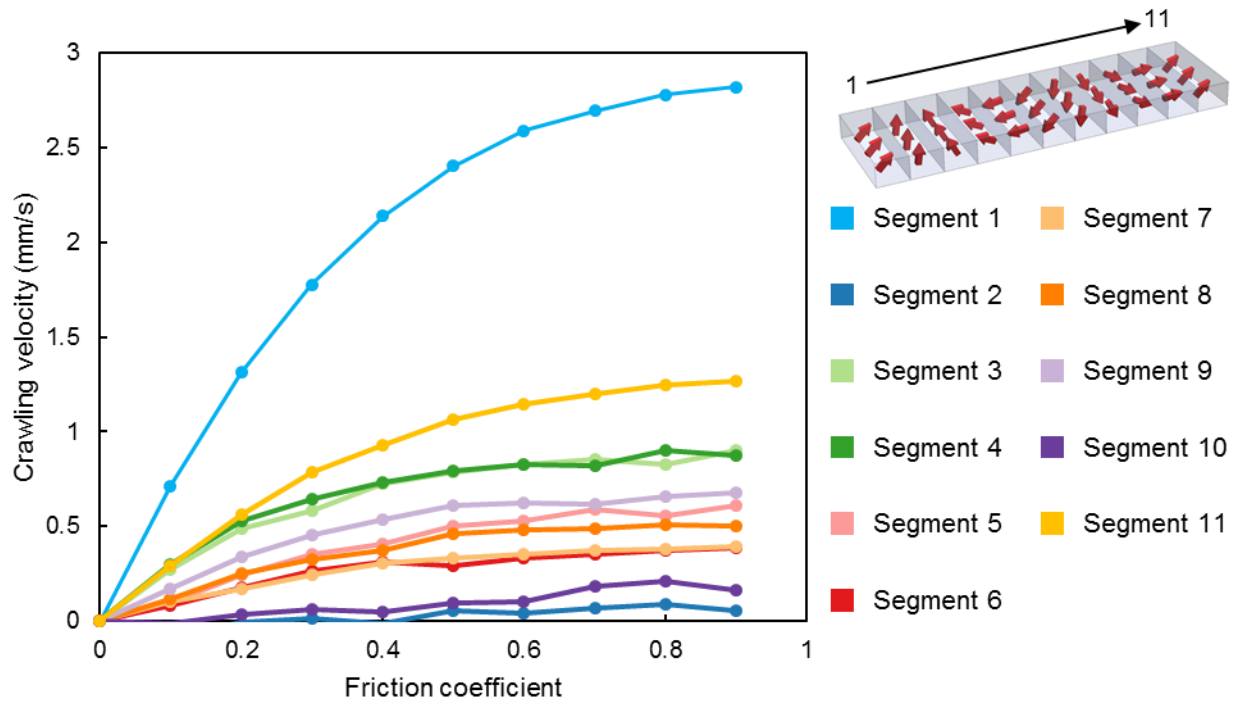


Fig. S7. The influence of the friction enhancement position at 11 segments along the robot length, investigated by CFD simulations. The simulated robot is divided into 11 equally-sized segments along its length. The crawling velocities are simulated at the conditions where only one of the segments is endowed with a friction coefficient while the others are set to be smooth. The friction coefficients vary within 0-0.9.

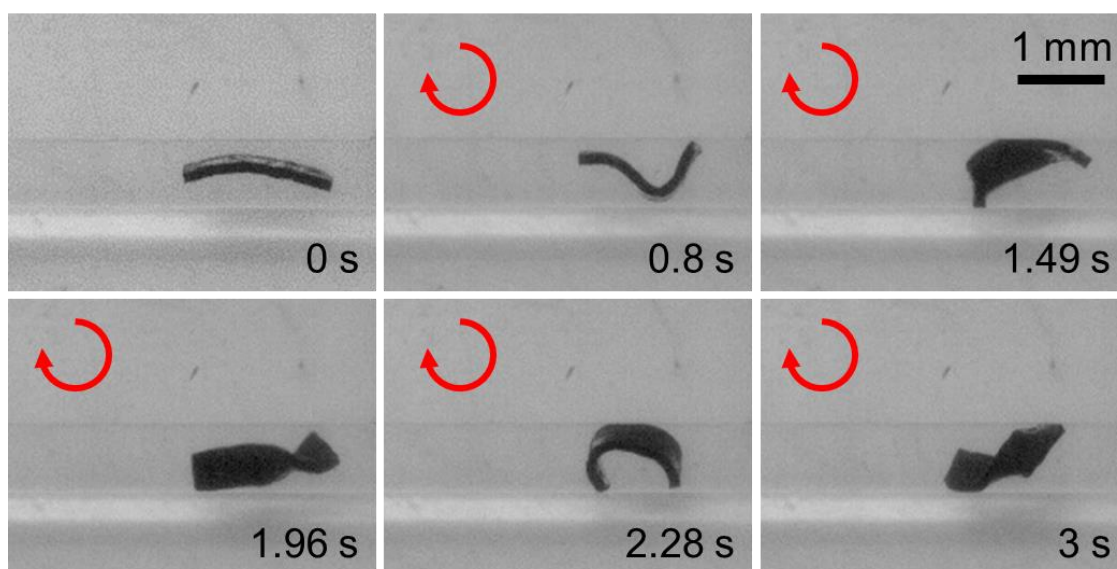


Fig. S8. The undulatory locomotion becomes unstable in a cylindrical tube. The red arrows indicate the direction of the in-plane \mathbf{B} field. The magnitude and frequency of the \mathbf{B} are 40 mT and 1 Hz, respectively.

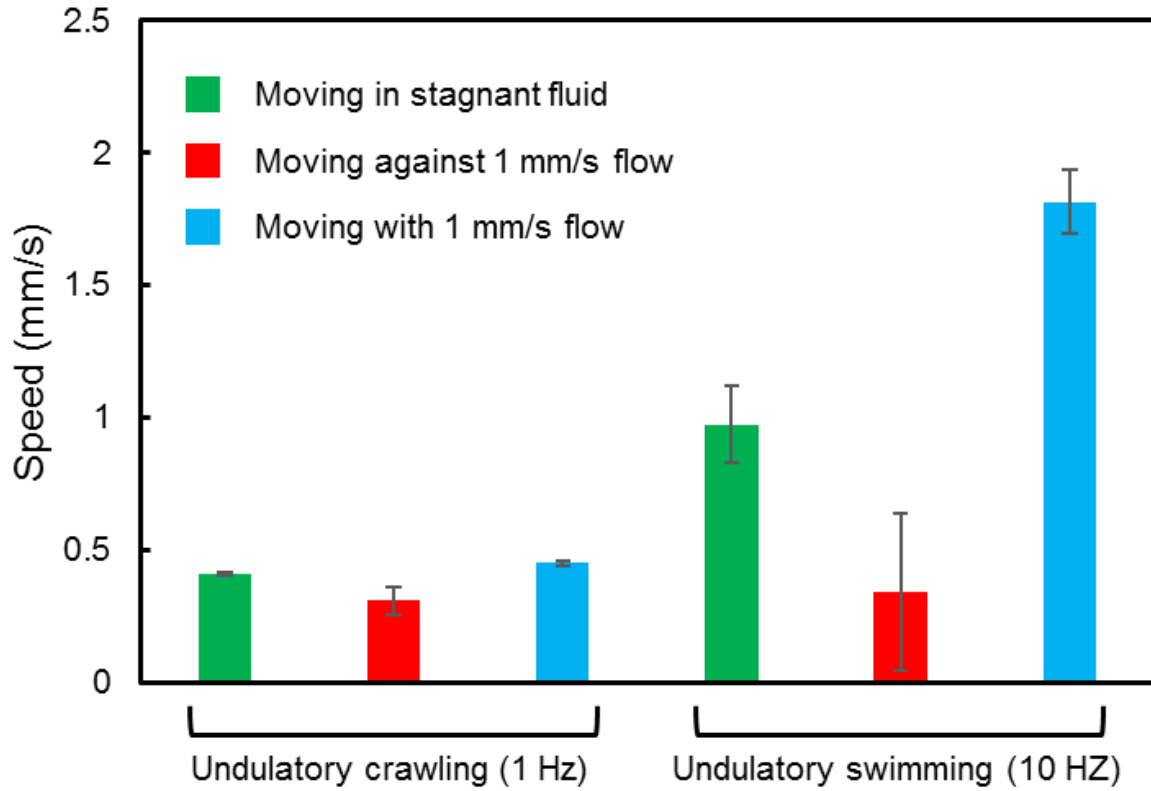
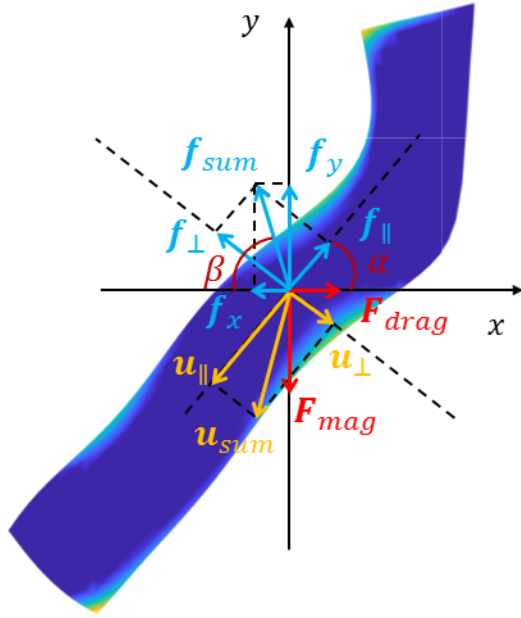


Fig. S9. Undulatory locomotion in flowing fluids. The undulatory swimming speed is much more sensitive to the background flow speed than the undulatory crawling. In undulatory crawling, the thrust force comes from the friction between the robot and the boundaries, and the robot can maintain the crawling motion as long as the friction is larger than the fluid load. However, in undulatory swimming, the existing of the background flow will always offset the swimming speed. In fact, compared to the swimming speed in stagnant fluid, the absolute mean swimming speeds changed by 0.63 mm/s and 0.84 mm/s in against-the-flow case and with-the-flow case, respectively. These changing values are at the same order as the background flow speed (1 mm/s). Further increasing the flow speed, such as 5 mm/s, will result in failure in undulatory locomotion especially when moving against the flow. This flow speed is much smaller than the stopping flow rate (10~56 mm/s) and drifting flow rate (27~420 mm/s) obtained from the helical surface crawling mode (Fig. 6A iv). The poor ability of the undulatory locomotion in moving in the fluid flow can be attributed to the large blocking ratio of the undulatory locomotion. To further enhance the performance of the undulatory locomotion in the flowing fluid as a future work, surface treatment could be conducted to the robot to increase its friction with the boundaries.

A Equilibrium state before creating grooves



B Equilibrium state after creating grooves

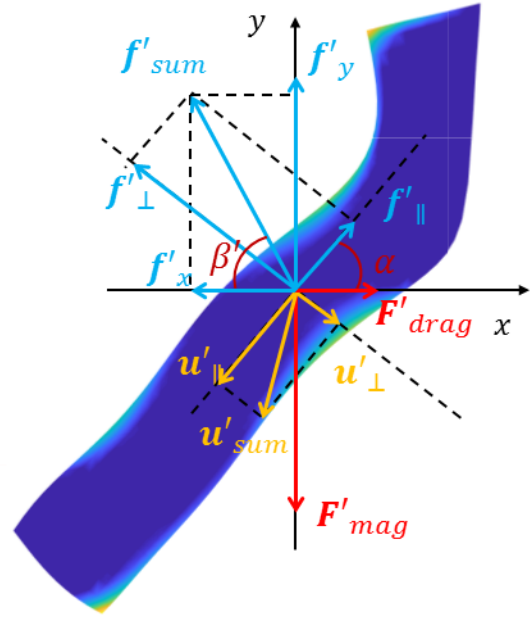


Fig. S10. Force analysis at the steady state of helical surface crawling. (A) The robot with a smooth surface. (B) The grooves are created on the robot to enhance the friction magnitude and the anisotropy. By introducing the grooves, the robot can acquire a larger thrust (f'_x).

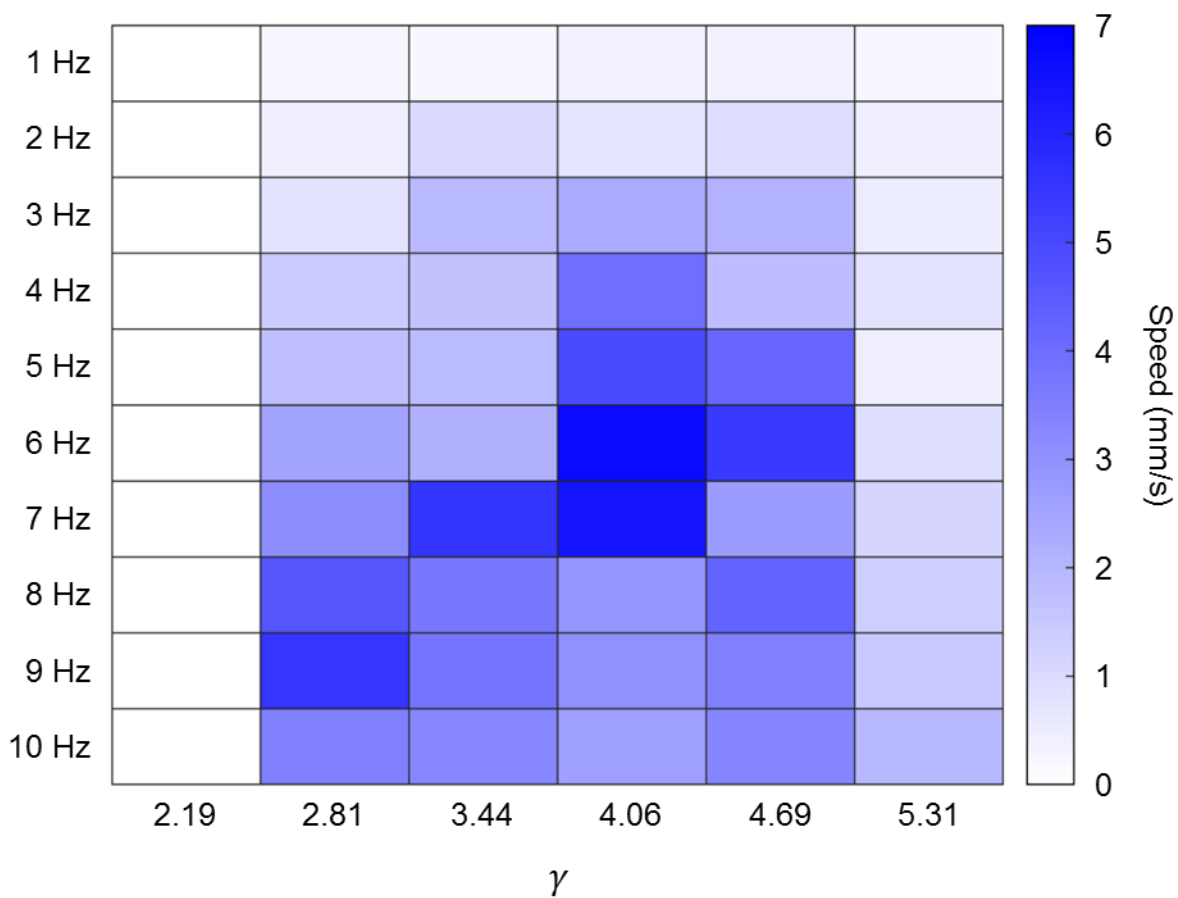


Fig. S11. Parameter sweeping experiments on helical surface crawling. The strength of the magnetic field is 40 mT, and $\eta=720$ cSt in all cases.

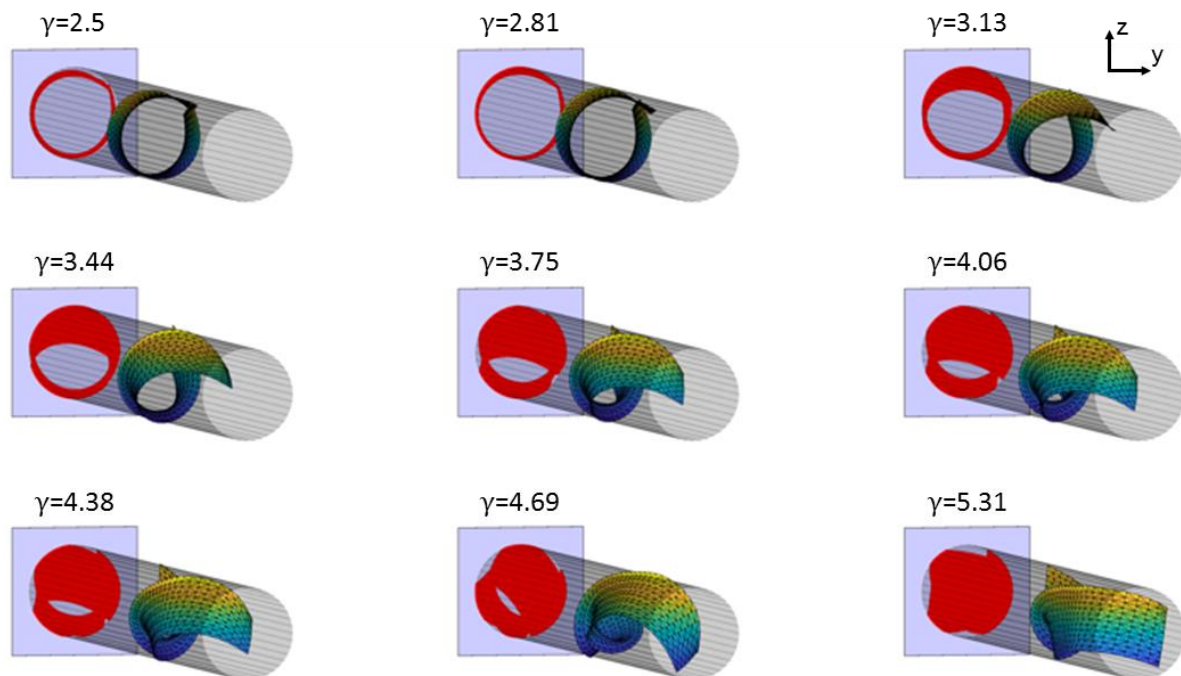


Fig. S12. The calculation of the blocking rate at different γ values in simulation. The blocking rate is defined as the projection area of the robot on the z - y plane (red area) divided by the cross-sectional area of the tube.

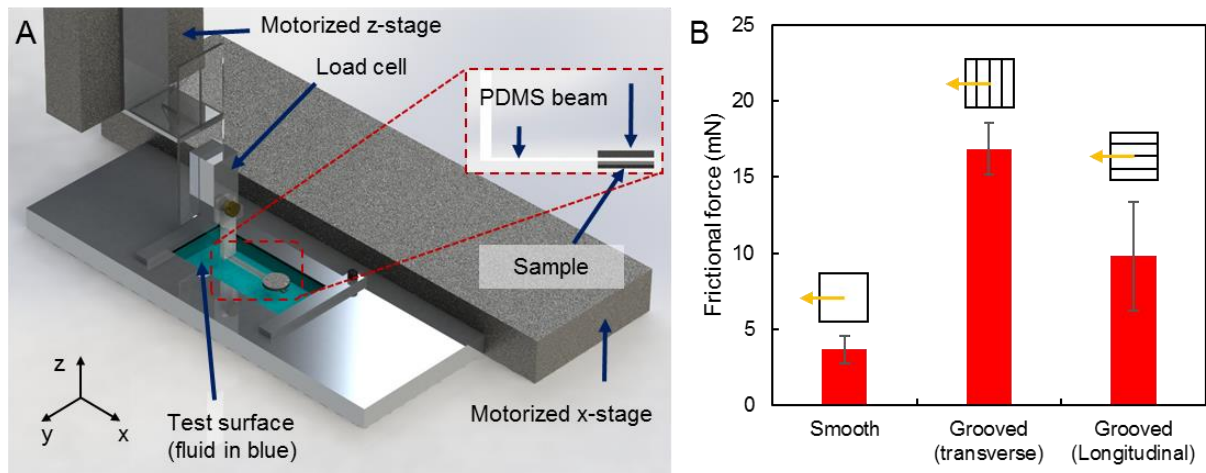


Fig. S13. Sliding friction measurement between the robot surface and the PDMS substrate for different conditions. (A) Schematic depicting the friction measurement set up. (B) The friction measured between the samples with different grooved patterns and the PDMS substrate. The samples were immersed in the glycerol during the measurement. The insets in (B) indicate the direction of the friction measurement.

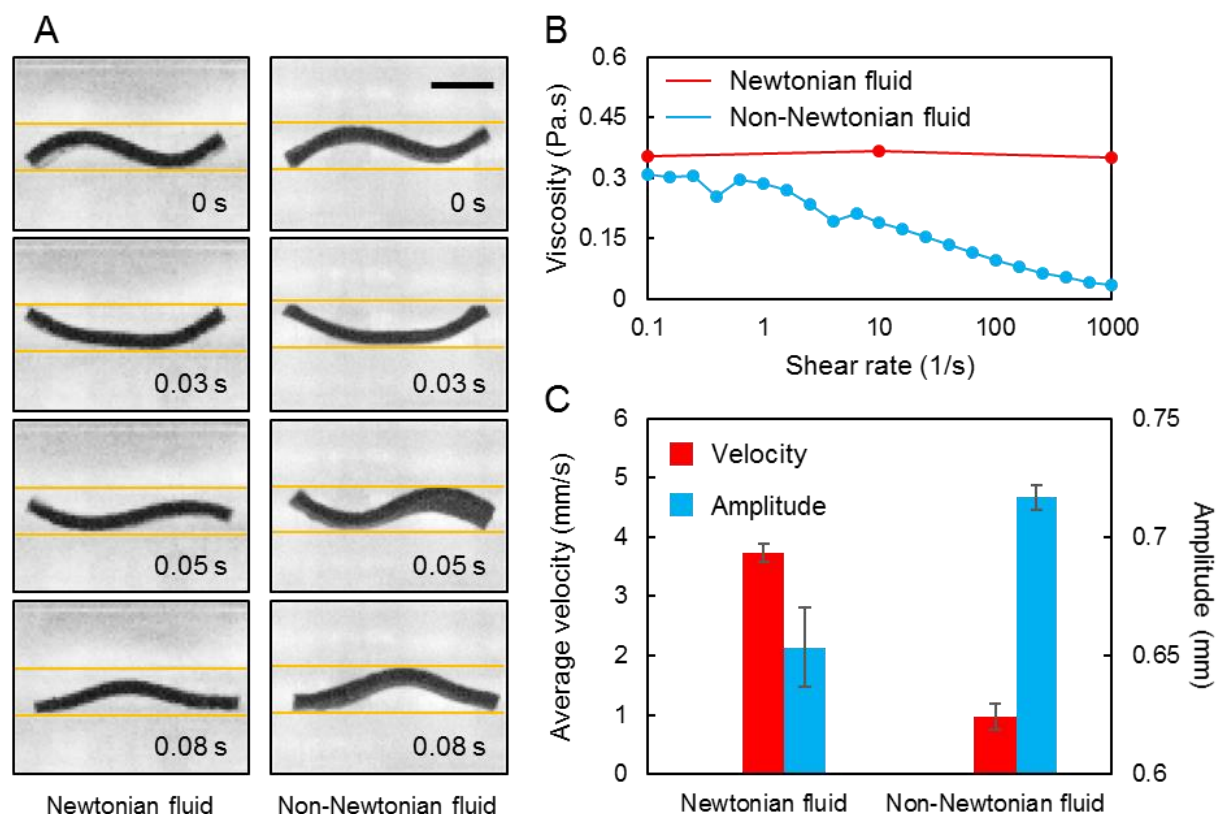


Fig. S14. Comparing the undulatory swimming performance in Newtonian and non-Newtonian fluids. (A) The deformations of the sheet-shaped soft robot during undulatory swimming (10 Hz) in Newtonian and non-Newtonian fluids, respectively. The yellow lines indicate the positions of the boundaries. The scale bar represents 1 mm. (B) The viscosities of the two fluids at different shear rate. The two fluids have similar viscosities at low shear rate, while the non-Newtonian fluid shows a significant shear-thinning property. (C) The average velocities and the undulation amplitudes of the robot swimming in two fluids.

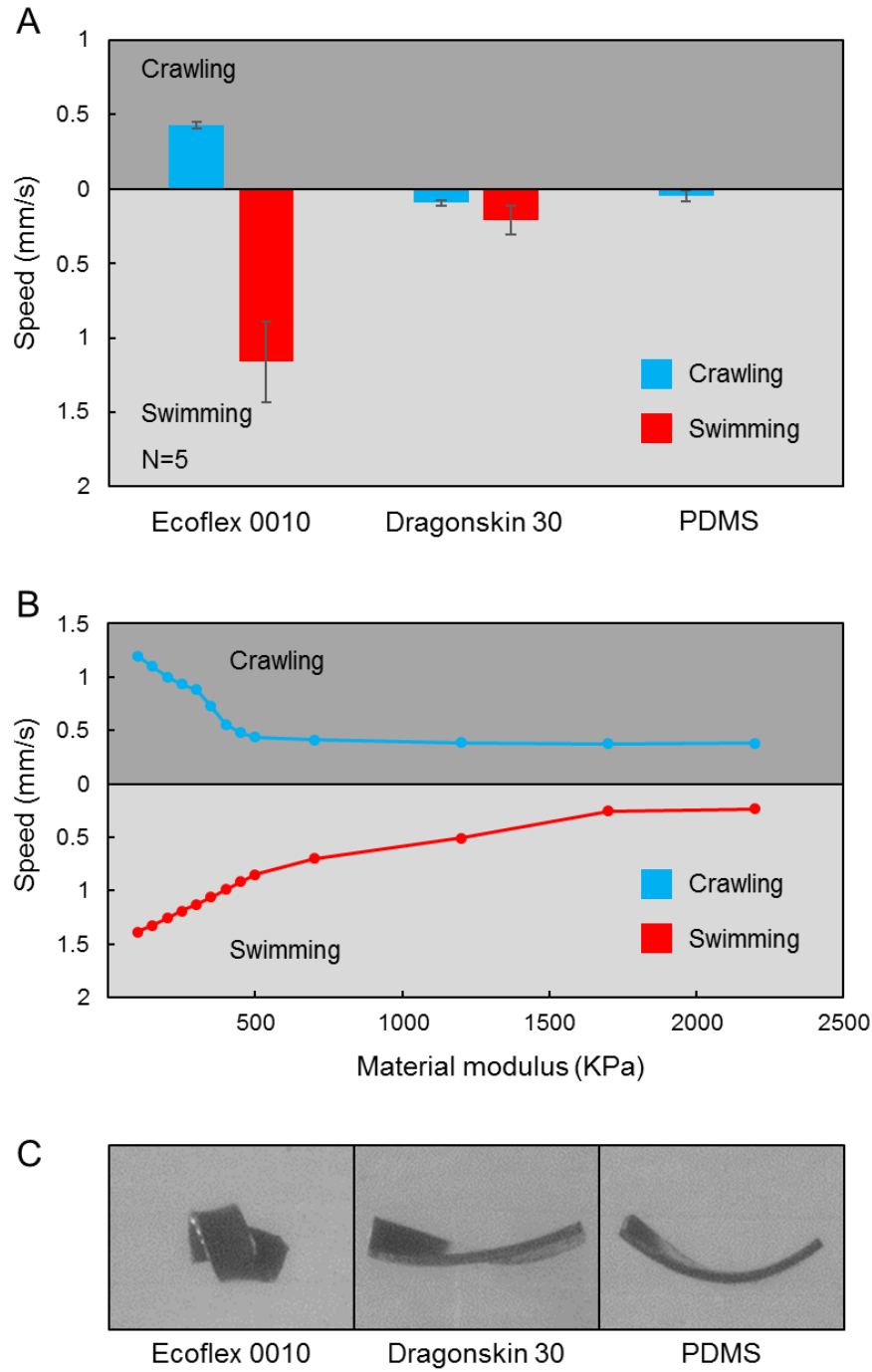


Fig. S15. The influence of the robot length and stiffness on moving speed. (A) The influence of the robot stiffness on undulatory locomotion speed investigated by experiments. (B) The influence of the robot stiffness on undulatory locomotion speed investigated by simulations. (C) The influence of the robot stiffness on helical surface crawling. The robot stiffness in (A)-(C) was tuned by changing the modulus of the magnetic composite material.

Supplementary Movies

Movie S1. Transition between undulatory crawling and swimming. The robot crawled at 1 Hz and 4 Hz while swam at 7 Hz and 10 Hz. The rotating direction of the magnetic field was kept unchanged so that the transmission direction of the undulatory body waves were the same.

Movie S2. Undulatory locomotion at different δ . The robot crawled at 1 Hz and swam at 10 Hz. The robot achieved the highest undulatory swimming and crawling speeds at $\delta = 4.67$. δ is defined as the ratio between the robot length and the gap width.

Movie S3. Undulatory locomotion with multiple waveforms. The robot crawled at 1 Hz and swam at 10 Hz. Multiple waveforms increased the undulatory swimming speed while did not change the undulatory crawling speed.

Movie S4. Maneuverability of the undulatory crawling. Scene 1: Crawling in ring-shaped channel. The robot with a shorter wavelength achieved a higher crawling speed. Scene 2: Taking the sharp turn. The robot with a longer wavelength got stuck at the sharp angle while the robot with a shorter wavelength successfully passed the sharp angle. Scene 3: Steering in a channel mimicking brain aqueduct. On-demand selection of the branch could be achieved by tuning the rotating direction and frequency of the magnetic field.

Movie S5. Helical surface crawling in a tube with fluid flow. The robot could crawl against and with the fluid flow or anchor in the tube to withstand flow when the magnetic field was turned off.

Movie S6. Helical surface crawling in a bending tube. The robot could be steered in a bending tube by aligning the rotating axis of the magnetic field to the local tangential direction of the tube. The bubble appeared in the tube did not influence the robot locomotion.

Movie S7. Helical surface crawling at different γ . The value of γ influenced the helical surface crawling speed. γ is defined as the ratio between the robot length and the inner tube diameter.

Movie S8. Multimodal locomotion in a phantom mimicking a dysfunctional Eustachian tube filled with middle ear effusion. Different locomotion modes were employed to adapt to local

environmental conditions. The phantom was filled with a shear-thinning non-Newtonian fluid. The shaking of the video is due to the vibration of the electromagnets.